The International Journal of Advanced Manufacturing Technology (2018) 96:491–501
https://doi.org/10.1007/s00170-018-1613-x

ORIGINAL ARTICLE

Effects of processing parameters on underfill defects in deep penetration laser welding of thick plates

Mingjun Zhang [1,2,3] · Kun Tang [1] · Jian Zhang [1] · Cong Mao [1] · Yongle Hu [1] · Genyu Chen [3]

Received: 28 July 2017 / Accepted: 10 January 2018 / Published online: 24 January 2018

Abstract
Underfill defect in welding affects not only the surface integrity but also the mechanical properties of workpiece. In this paper, the effects of the process parameters on underfill defects were investigated, and the deep penetration welding by a 10-kW fiber laser on 12-mm-thick stainless steel plates was used as the case study. The correlation of the processing parameters with the formation and elimination of underfill defects was analyzed and discussed. It was found that during the autogenous laser welding of thick plates, the direction of laser beam relative to gravity has a significant effect on the formation of underfill defects, and the preferable direction was an inclination angle of 60° with respect to the gravity. A negative defocus tended to obtain a full penetration weld with underfill and undercut defects. The higher the welding speed was, the lower the underfill depth was on the top surface. This phenomenon was observed on the full penetration welds at a defocus of − 10 mm. With a negative defocus, it became feasible to optimize the combination of the focal position and the welding speed to achieve a satisfactory appearance of welds. In addition, a bottom-shielding ambience helped the full penetration in the laser welding process positively.

Keywords Fiber laser welding · Thick plate · Underfill defects · Processing parameter · Parameter optimization

1 Introduction

Modern high-power fiber and disc laser sources enable a stable single-pass welding process even for thick plates [1–8]. For examples, Bachmann et al. [1] carried out experimental and numerical investigation on thick-plate welding; they used a 20-kW fiber laser to conduct a full penetration laser welding on a 30-mm-thick aluminum plates with an electromagnetic weld pool support system. Zhang et al. [2] investigated the influence of the processing parameters on the weld bead geometry; a 10-kW fiber laser was used to weld thick-section stainless steels. When a 16-kW disc laser was used to conduct autogenous laser keyhole welding on low-alloyed steels, Sokolov et al. [3] found that the penetration depth was increased significantly, especially, in partial vacuum atmospheric conditions. Guo et al. [4] and Shen et al. [5] compared the characteristics of high-power fiber laser welding of 13-mm-thick steel in flat and horizontal positions. Sun et al. [6] proposed a new welding technique for welding thick stainless steels horizontally; this was achieved by a combination of the autogenous laser welding and laser welding assisted with a cold wire.

However, a large number of experiments in laboratories and factories have proved that when a high-power fiber laser is used to weld thick plates with full penetration, it is very difficult to control the weld appearance. Some common defects of weld appearance are surface underfill, undercut, root sagging, and spatters [9–11]. Many researchers have investigated the causes and formations of these weld defects. Yang et al. [12] confirmed that narrow welding pool, less molten metal, poor liquid metal backfilling ability, as well as high cooling rate resulted in underfill during autogenous laser welding of 3-mm aluminum alloy. Guo et al. [4] demonstrated that surface

✉ Mingjun Zhang
hnuzmj@163.com; mj_zhang@csust.edu.cn

[1] Key Laboratory of Lightweight and Reliability Technology for Engineering Vehicle, Education Department of Hunan Province, Changsha University of Science and Technology, Changsha 410114, People's Republic of China

[2] School of Energy and Power Engineering, Key Laboratory of Efficient and Clean Energy Utilization, Changsha University of Science and Technology, Changsha 410114, China

[3] State Key Laboratory of Advanced Design and Manufacturing for Vehicle Body, Hunan University, Changsha 410082, People's Republic of China

underfill was caused by a gravity-induced fluid which flowed toward the root of the weld; it was found when an autogenous fiber laser welding was applied on 13-mm-thick high strength low alloy (HSLA) steel plates horizontally. Matsumoto et al. [13] showed that during the high-power fiber laser welding of a 12-mm-thick high-strength steel plate, a full penetration weld with deep underfill defects was generated on the top or bottom surface of the weld beads. Li et al. [14] found that the underfilled weld was attributed to formation of spatter at the root of weld pool.

A number of techniques (such as using a filler wire) have been proposed to reduce the number of underfill defects. For examples, Kashaev et al. [15] proposed to use an alloy compatible filler wire to avoid underfills and undercuts during laser welding of Ti–6Al–4 V butt joints and T-joints. Fang et al. [16, 17] developed a transversal pre-extrusion method to reduce underfill during laser welding of thin titanium alloy plate. Zhang et al. [18] analyzed the formation mechanism of weld defects such as spatter, underfill, and undercut for laser welding of 1.5-mm-thick copper butt joint, and suggested that the appearance of the full penetration welded joints could be improved with a high welding speed and a specified laser power. Pan et al. [19] found that the underfill, undercut, and hump defects could be suppressed with a proper value of laser power, welding speed, and arc current during laser-arc hybrid welding of thick plate.

Direct observation of the keyhole geometry is not feasible when welding nontransparent materials such as metals. Several experimental investigations were carried out to determine whether the dynamic keyhole shapes produced during deep penetration laser welding of various metals could be observed using an X-ray transmission imaging system with a high-speed video camera [20, 21]. Welding experiments employing water and ice [22] have been performed to observe the capillary behavior and the flow field in the weld pool, even though there are significant differences in the material properties of water and metals. A special transparent material, borosilicate glass (GG17), has been exploited to observe the keyhole in deep penetration laser welding [23, 24]. In our previous work, the keyhole wall has been captured by using a high-speed imaging system during fiber laser welding of a modified sandwich specimen [25]. Recently, the micromorphology of the keyhole wall has been measured via a scanning electron microscope [26, 27]. The keyhole shape and the conversion of laser energy in the keyhole during laser welding are research focuses all the time [27–29].

In the present study, the effects of the processing parameters on the underfill were investigated, especially, the formation and elimination of underfill were analyzed from the perspective of processing technique. As a case study, a 10-kW fiber laser was used for an autogenous laser welding on a 12-mm-thick stainless steel plates.

2 Experimental procedures

Figure 1 shows the setup of the experiments. The laser source was a continuous wave fiber laser (IPG YLS–10000) with a maximum power of 10 kW. The laser beam had the product of 7.5-mm·mrad with a processing fiber 200 μm in diameter. The laser beam emitted from the end of the optical fiber was collimated by a lens with a focal length of 150 mm and was then focused on the specimen surface using a lens with a focal length of 300 mm.

The material used was Type-304 austenitic stainless steel with the thicknesses of 12 mm. Table 1 gives the chemical composition of the base material. The modified "sandwich" sample consisted of one sheet of stainless steel with the size of $40 \times 12 \times 5$ mm^3 and one sheet of GG17 glass with the same size. The setup for high-speed imaging experiments in the literature [30] was adopted here. Interested readers might find the details about "sandwich" plates and experiment setup in [30]. Two types of shielding gas, i.e., nitrogen and argon, were used during bead-on-plate welding experiments.

Figure 2 shows a schematic representation of the laser welding setup for different welding positions. The inclination angles between the incident laser beam and gravity direction were 0°, α, 90° for flat, downhill, and vertical-down welding positions, respectively. During downhill welding, the inclination angles α were 15°, 30°, 45°, 60°, and 75°.

After welding, typical cross sections of the samples were cut by electrodischarge machining (EDM). Then, the samples were polished with abrasive paper as well as diamond slurry and were finally etched by a solution of aqua regia ($HCl:HNO_3 = 3:1$) for 15 s to reveal the microstructure of the joints, which was observed with a metalloscope (LEICA MEF3A). The macrostructure of the joints was observed with a stereoscope (LEICA S6 D). The underfill depth on the longitudinal section of joint was measured via the native software of the stereoscope directly. The area of underfill zone was computed by using binarization processing for the longitudinal sectional image in the MATLAB software, and thereby the average underfill depth was calculated.

3 Results and analysis

3.1 Effects of processing parameters on the formation of underfill

3.1.1 Welding position

Figure 3 shows the effect of the welding position on the longitudinal sections of joints welded at a laser power of 10 kW, the defocus of − 10 mm, the welding speed of 1.5 m/min, and with the top-shielding gas flow of 30 l/min (N_2). Figure 4 gives the relationship of the underfill depth with the welding

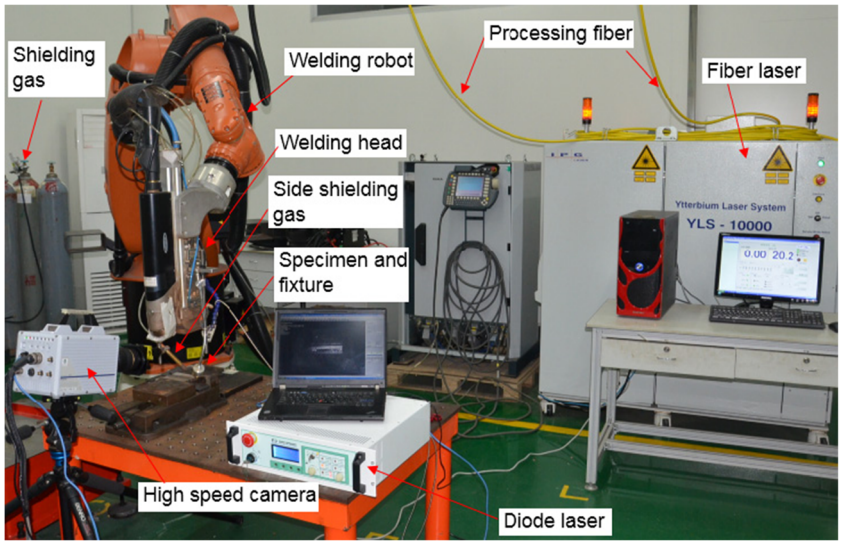

Fig. 1 Setup of experiment

position. As can be seen from Figs. 3a and 4, the maximum underfill depth and the average underfill depth in the horizontal position of welding were 2.288 and 1.095 mm, respectively. When the welding position was changed from horizontal position into downhill position with an inclination angle of 15°, the maximum underfill depth and the average underfill depth decreased significantly, and the maximum underfill depth occurred at the end of the weld, which is shown in Figs. 3b and 4. As the inclination angle was increased from 15° to 60°, the underfill depth values decreased continuously, and the longitudinal sections of the welds became uniform without obvious depression at the top surface, as shown in Figs. 3c–e and 4. When the inclination angle was increased to 90°, namely the vertical-down welding position, the maximum underfill depth increased moderately while the average underfill depth decreased slightly, which is shown in Figs. 3f, g and 4. The maximum underfill depth occurred at the start of the weld.

3.1.2 Focal position

Figure 5 illustrates the weld appearance and cross sections of joints welded at different focal positions with a laser power of 10-kW, the welding speed of 1.5 m/min, and with the top-shielding gas flow of 30 l/min (N_2). As one can see from Fig. 5, the partial penetration welds were obtained with the defocus value of zero or plus five. Undercut and spatter defects occurred on the top surface. The full penetration welds were achieved with the defocus value of minus five or minus ten. Particularly, at a defocus of minus five, a uniform deep underfill and several root humps were formed on the top surface and bottom surface, respectively. When the defocus was reduced to minus ten, a shallow underfill was observed on the top surface, and an undercut was found on the bottom surface at the first half part of the weld. However, a deep depression occurred on the top surface, and a root hump was formed on the bottom surface at the middle part of the weld, correspondingly. On the basis of our previous result [30], it was reasonable, since the deep underfill was generated accompanying with the formation of the root hump, and the root hump was caused by the transition of the welding mode from full penetration of keyhole to full penetration of melt. This was attributed to the escape of the pressurized energized vapor plume and the laser loss through the open keyhole.

Table 1 Chemical composition of specimen materials

Element	C	Mn	P	S	Si	Cr	Ni	N	Fe
(Wt.%)	0.07	2.00	0.045	0.03	0.075	18.28	8.15	0.1	Balance

3.1.3 Welding speed

Figure 6 shows the correlation of the welding speed with the welds on the longitudinal sections of joints subjected to a laser power of 10 kW, the defocus of − 10 mm, and with the top-shielding gas flow of 30 l/min (N_2). Figure 7 illustrates the relationship of the underfill depth with the welding speed. At the welding speed of 1.2 m/min, the maximum underfill depth occurred at the position, where root hump was formed on the bottom surface, which is shown in Fig. 6a. Besides, the maximum underfill depth and the average underfill depth were 2.731 mm and 2.02 mm, respectively, which were shown in Fig. 7. It was reasonable to conclude that the formation of root hump at the bottom surface absorbed a large number of molten metal downward, resulting in a deep underfill on the top surface [31]. When the welding speed was increased to 1.5 m/

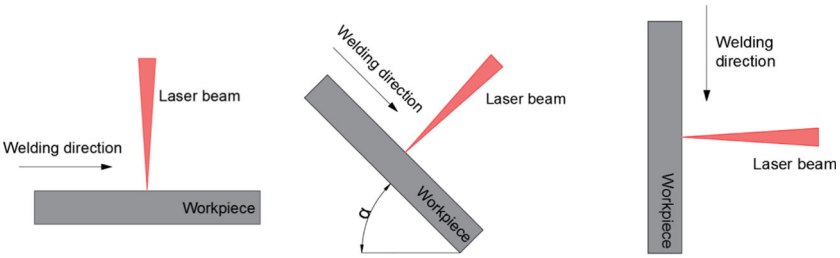

(a) Flat welding position (b) Downhill welding position (c) Vertical–down welding position

Fig. 2 Schematic representation of the experimental setup with different welding positions. **a** Flat welding position. **b** Downhill welding position. **c** Vertical-down welding position

min, both the maximum underfill depth and the average underfill depth decreased significantly, which are shown in Figs. 6b and 7, respectively. As the welding speed was increased to 2.1 m/min, the underfill depth values were further decreased, and the longitudinal sections of the welds became uniform on the top and bottom surfaces, which are shown in

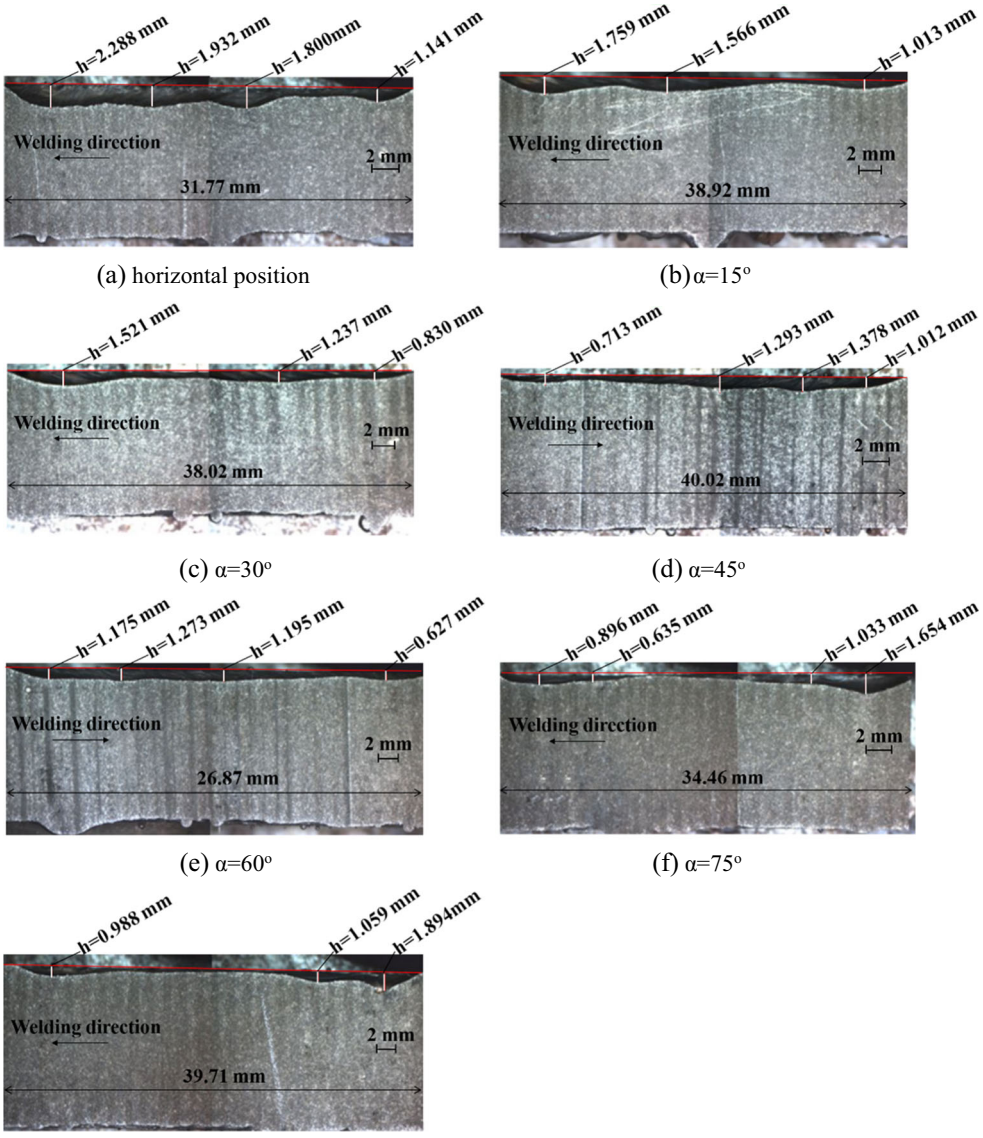

(a) horizontal position (b) α=15°

(c) α=30° (d) α=45°

(e) α=60° (f) α=75°

(g) Vertically–down position

Fig. 3 Longitudinal sections of joints welded at different positions of welding

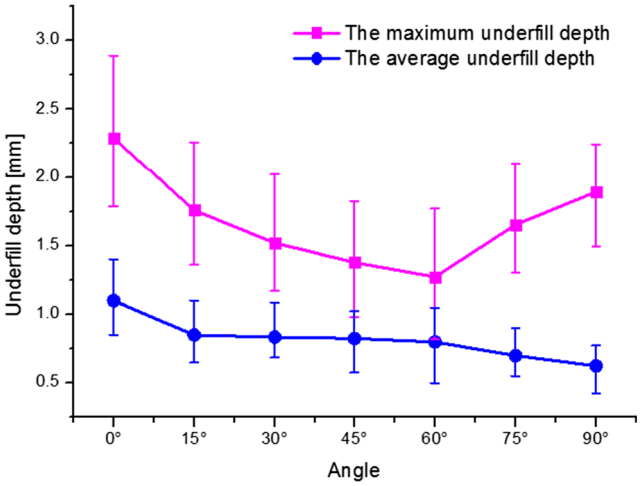

Fig. 4 The effect of welding position on the underfill depth

Figs. 6c, d and 7. The maximum underfill depths occurred at the end of the welds as shown in Figs. 6b–d.

3.2 Process optimization

The aforementioned experimental results have shown that in using the high-power fiber laser on thick plates, two critical

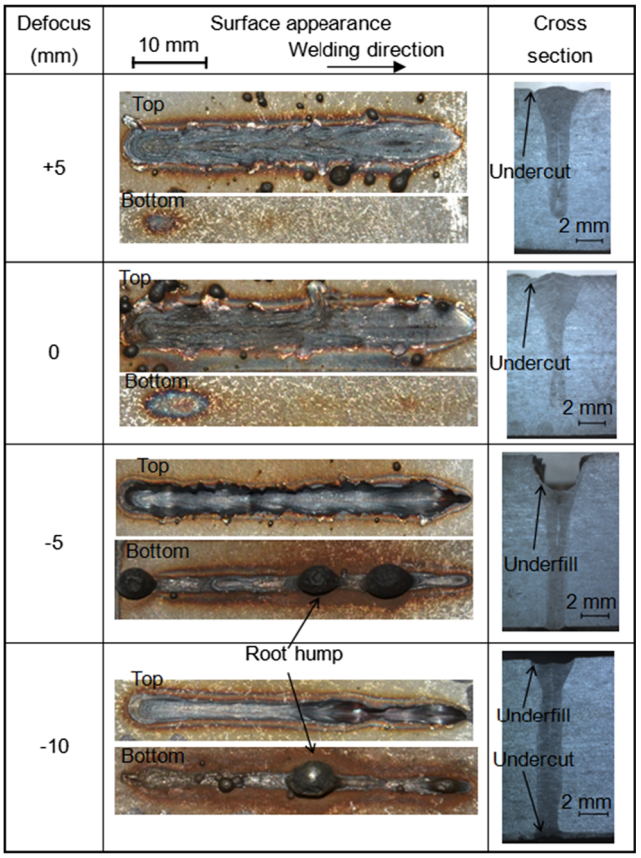

Fig. 5 Weld appearance and cross sections of joints welded at different focal positions [2]

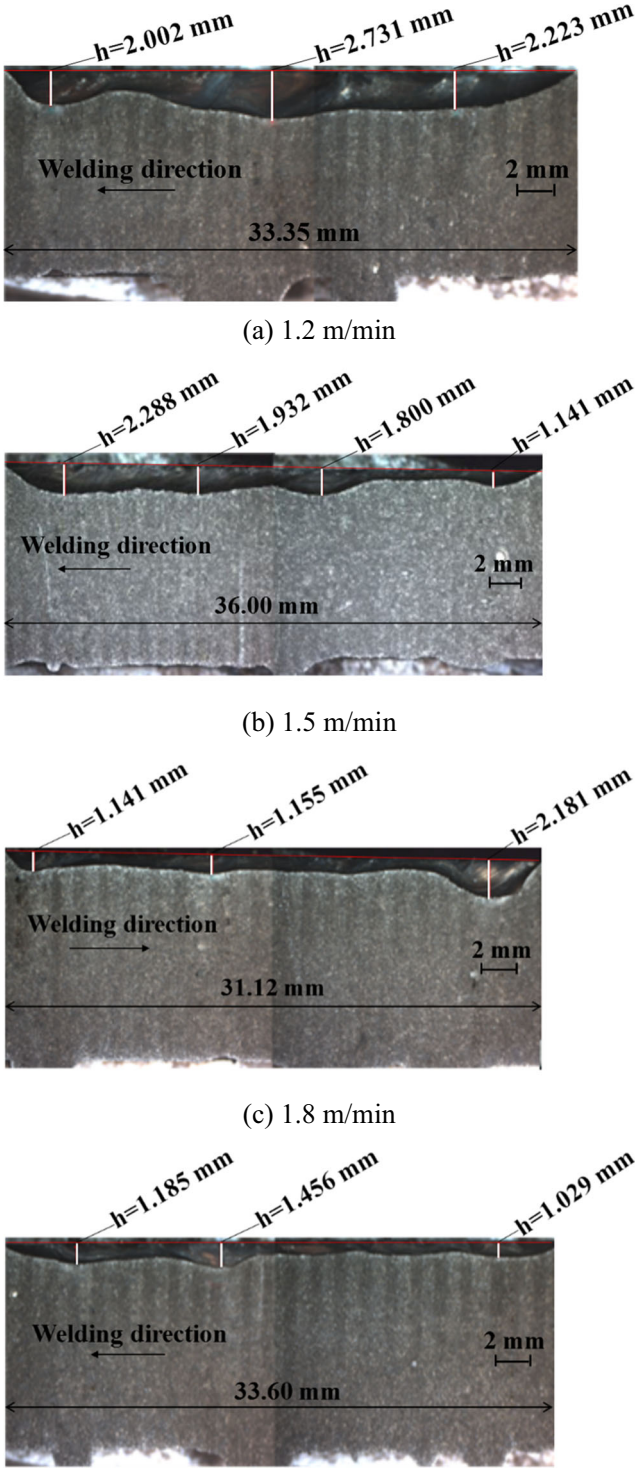

Fig. 6 Longitudinal sections of joints welded with respect to welding speed

welding parameters are the focal position and the welding speed. Figure 8 shows the variation of the weld penetration and cross section with respect to the defocus value and welding speed. It could be found that, for a positive defocus

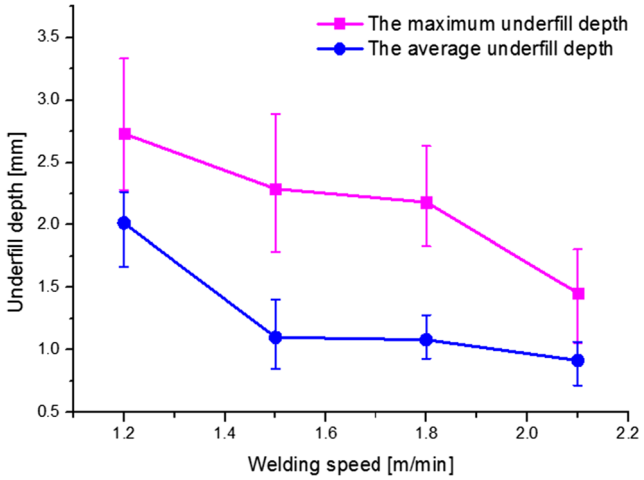

Fig. 7 The effect of welding speed on the underfill depth

or zero defocus, the upper surface of the weld collapsed slightly and the bottom hump appeared on the lower surface, and the cross section of the weld presented as a typical glass-type weld under low-speed full penetration welding. However, when the welding speed was increased slightly, the upper surface of the fully penetrated weld collapsed severely, and the bottom hump was very large on the lower surface. As a consequence, the weld appearance was extremely poor. If the welding speed was increased continuously, the welding process would immediately be changed into non-penetration welding which was easy to produce surface spattering and nail head weld. In summary, the results in Fig. 8 show that it was infeasible to obtain a well-formed weld through the change of the defocus value and the welding speed subjected to a positive or zero defocus.

For a negative defocus, during the low-speed full penetration welding, the upper surface of the weld collapsed, while the lower surface stayed unchanged. Instead, there was a partial concave, and the cross section of the weld appeared as a typical nail head weld. With an increase of the welding speed, the upper surface of the weld collapsed, and the lower surface sags and the nail head weld gradually disappeared. With the further increase of the welding speed, the collapse in the upper surface of the weld tended to be reduced, and the nail head weld almost disappeared, and the weld presented as an "I" type weld. Hereafter, if the welding speed was further increased, the welding process was changed into non-penetration welding, and there would be a small amount of small spatters on the upper surface of the weld. The weld width was narrow, and there was no obvious nail head weld. As a summary, for a negative defocus welding, it was feasible to obtain a well-formed weld through the change of the defocus amount and the welding speed, and there was an optimal combination of the defocus value and the welding speed.

Figure 9 shows the weld appearance and cross section of the butt joint. The welding parameters are with a laser power

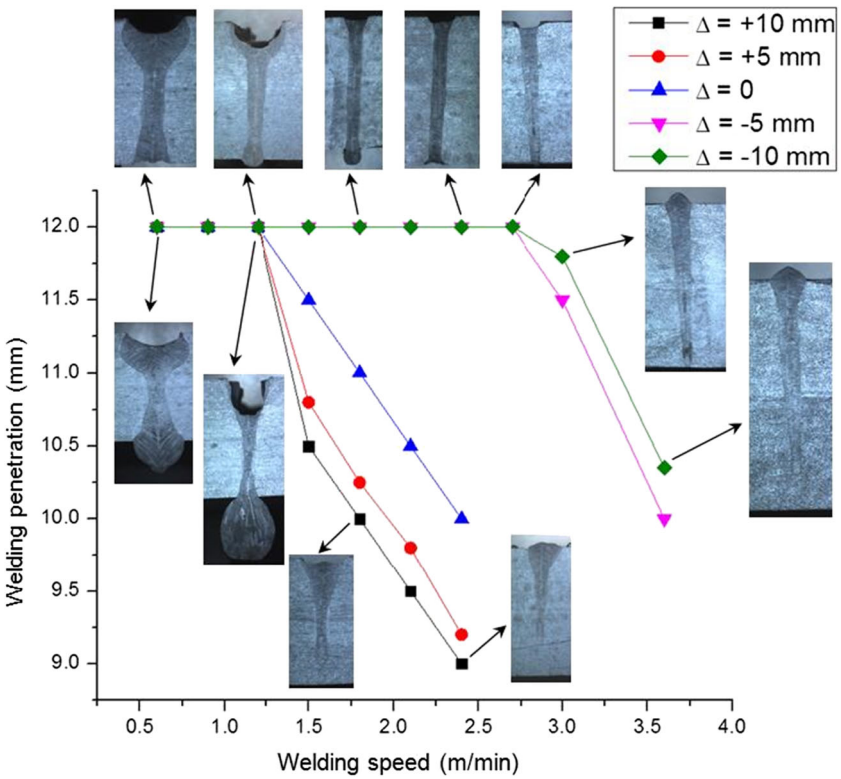

Fig. 8 The variation of weld penetration and cross section with respect to defocus value and welding speed

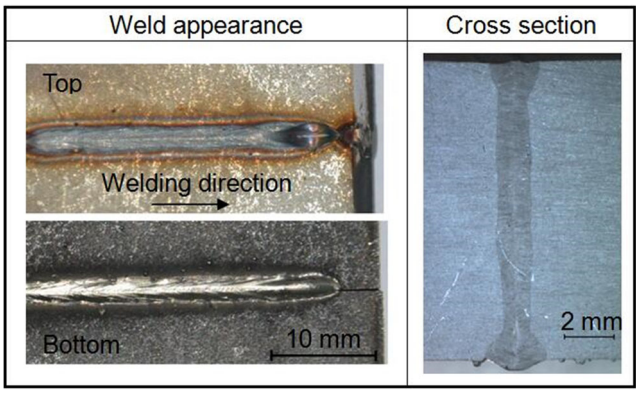

Fig. 9 Weld appearance and cross section of the butt joint with bottom-shielding argon gas

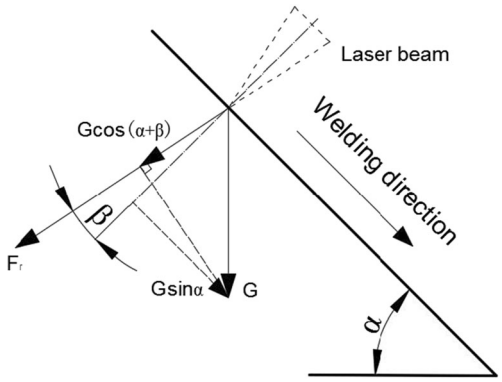

Fig. 10 Schematic of force condition at front keyhole wall

of 10 kW, the defocus of − 10 mm, the welding speed of 2.1 m/min, and with the top-shielding gas flow of 30 l/min (N_2), and bottom-shielding argon gas flow of 5 l/min (Ar). As could be seen from Fig. 9, the weld appearance on the top and bottom surfaces was in good shape without an obvious underfill defect, and an "I" shape cross section of the butt joint was formed [32]. It was easily explained that a bottom-shielding ambience for the full penetration laser welding of thick plates was not only conducive to stabilizing the welding process but also helpful to achieving an excellent weld appearance on the top and bottom surfaces.

4 Discussion

Figure 10 shows the force condition at the front keyhole wall during the downhill welding. In the figure, F_r was the recoil pressure induced by the evaporation of material at the front keyhole wall, α was the inclination angle between the incident laser beam and the gravity, β was the inclination angle of the front keyhole wall compared with the laser beam axis, and G was the gravity of melt pool. When the angle α was small, the component force ($Gsin\alpha$) of the gravity in the welding direction was less and had less influence on the melt flow in the welding direction. However, as the angle α was increased gradually, the component force ($Gsin\alpha$) of the gravity in welding direction was increased as well, and had the significant influence on the melt flow in the welding direction. Consequently, the maximum underfill depth occurred at the start of the weld, which is shown in Figs. 3f, g. On the other hand, at a small angle of α, the component force ($Gcos(\alpha + \beta)$) of the gravity in the direction of the force F_r was large and had an facilitation action on the downward flow of the melt pool to form underfill on the top surface, which is shown in Figs. 3a and 4. However, with the angle α was increased gradually, the component force ($Gcos(\alpha + \beta)$) of the gravity in the direction of the force F_r was decreased and had a less facilitation action on the downward flow of the melt pool to form underfill on the top surface, as shown in Figs. 3b–g and 4. Especially, when the sum of angle α plus angle β was bigger than 90°, the component force ($Gcos(\alpha + \beta)$) of the gravity in the direction of the force F_r turned into minus value. In this case, the component force ($Gcos(\alpha + \beta)$) of the gravity could partially counteract the downward flow driven by the recoil pressure F_r. As a result, the underfill defect on the top surface was improved, and the average underfill depth was reduced, which are shown in Figs. 3f, g and 4.

Figure 11 shows a schematic of the geometrical optical propagation produced by multiple reflections of the laser beam on the keyhole wall under different focusing states. It was seen in the figure that the reflection position of the laser beam on the keyhole wall was related to the incident angle Φ of the laser beam. When $\Phi < 90° - \alpha$, that was, the laser beam was in the outward divergent state, the first reflection of the laser beam on the hole wall propagated close to the opening of the keyhole, the depth of the light propagating downward was limited. Thereafter, the light was reflected toward the opening of the keyhole upon the second reflection of the laser beam on the keyhole wall. Finally, the light was directly reflected to the outside of the keyhole after the third reflection, which is shown in Fig. 11a. When $\Phi > 90° - \alpha$, that was, the laser beam was in the state of inward convergence, the laser beam was propagated to the depth of the keyhole after the first reflection on the keyhole wall propagated close to the opening of the keyhole. Upon the second reflection, it was still in the depth of the keyhole followed by the upward propagation of the light, but after the third reflection, the position of light propagation was changed into the middle of the keyhole, which is shown in Fig. 11b. Obviously, for the positive defocus welding, the focal position was above the surface of the material, the laser beam irradiated the surface of the material, and the keyhole wall in a divergent state. The Fresnel absorption generated by multiple reflection of the laser beam on the keyhole wall mainly occurred near the opening of the keyhole. However, for the negative defocus welding, the focal position was below the surface of the material, the laser beam irradiated the surface of the material, and the keyhole wall in a convergence state [33].

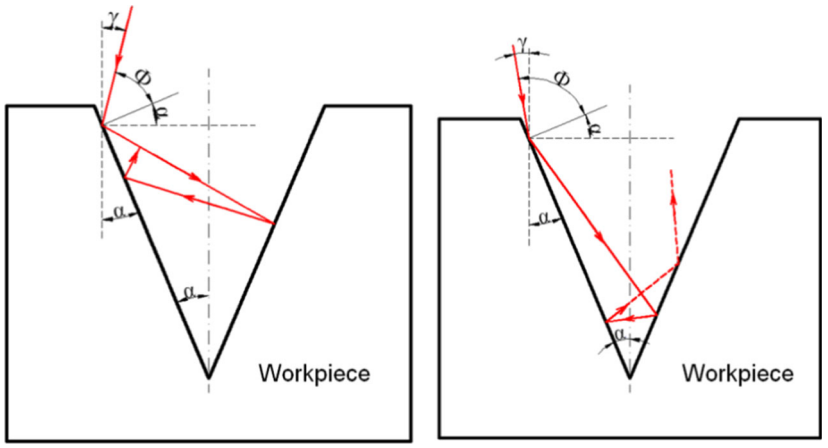

(a) Outward divergent laser beam (b) Inward convergent laser beam

Fig. 11 The geometrical optical schematic of the multiple reflection of the laser beam on the keyhole wall under different focusing states. **a** Outward divergent laser beam. **b** Inward convergent laser beam

The Fresnel absorption generated by the multiple reflection of the laser beam on the keyhole wall occurred in the depth of the keyhole [23]. The laser power density absorbed on the lower keyhole wall was related to the multiple reflection of the laser beam in the keyhole [34]. Therefore, the change of the defocus value affected the distribution of the laser power absorbed on the keyhole wall, and thus, changed the shape of the keyhole.

Figure 12 shows the images of the longitudinal keyhole during fiber laser welding of the modified sandwich sample at a laser power of 10 kW under the welding speed of 3 m/min. It can be seen from Fig. 12a that during positive defocus welding, the front keyhole wall was inclined obviously, and there was local evaporation on the upper and lower keyhole wall with a large opening. Nevertheless, when the defocus value was negative, the inclination angle of the front keyhole wall was small and was almost vertical, and the local evaporation occurred on the lower keyhole wall with a large keyhole bottom and a keyhole with deep depth, which is shown in Fig. 12b. Apparently, negative defocus was conductive to obtaining a deeper and more stable keyhole, which facilitates obtaining a good weld.

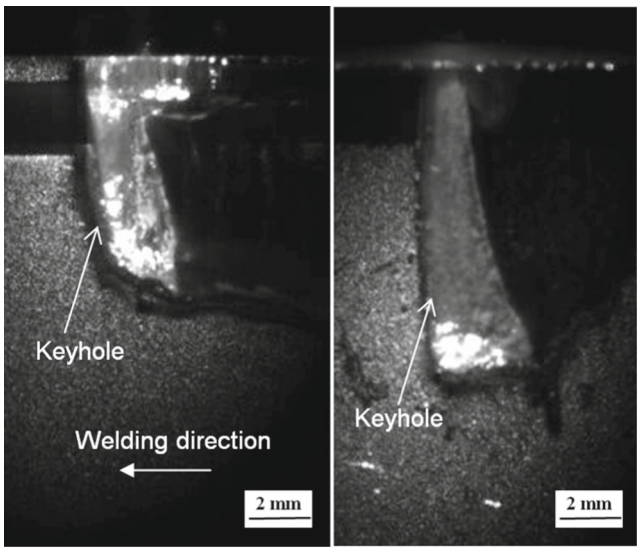

(a) Δ=+10 mm (b) Δ=−10 mm

Fig. 12 Images of longitudinal keyhole with respect to defocus values in fiber laser welding of the modified sandwich sample

Figure 13 illustrates the high-speed observation images and schematic of the weld pool, metallic vapor, and keyhole behavior at different welding speeds. It can be seen from Fig. 13a that the keyhole aperture was surrounded by a substantial molten metal with the formation of a melt "crown" when the welding speed is low. On the other hand, the keyhole was near vertical, and the keyhole wall was prone to producing wrinkles and liquid shelf. As for the fiber laser, the local evaporation on the upper surface of the wrinkles or the liquid shelf was intense, resulting in metallic vapor, which was of high-speed and jets upward. During partial penetration welding, a substantial melt volume accumulated at the top of melt pool, resulting in a well-known nail head shape weld [35]. However, once full penetration was achieved, the molten metal had a rather large melt pool with limited hydrodynamics, and it flowed downward to sag below the bottom surface of the workpiece under the action of gravity and surface tension effects [31, 36–38]. Consequently, an underfill on the top surface of the weld and root hump on the bottom surface was formed. With the increase of the welding speed, the molten metal pat on the front wall of the keyhole was thinner, and wrinkles and liquid steps on the keyhole wall were not obvious as shown in Fig. 13b. Meanwhile, the inclined front wall of the keyhole evaporated acutely under the direct irradiation of the laser beam. The metallic vapor induced from evaporation jets backwards and expanded the opening of the keyhole, which in turn facilitated the removal of the metallic vapor inside the keyhole, thus maintaining the stability of the keyhole and efficiently preventing welding defects [39, 40].

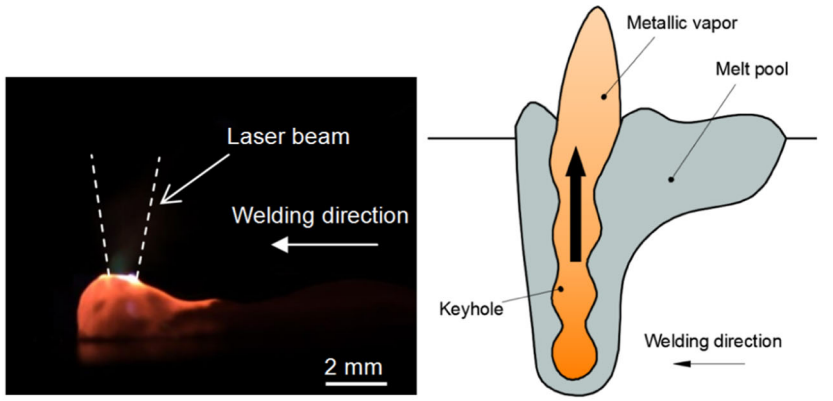

(a) v ≤ 1.5 m/min

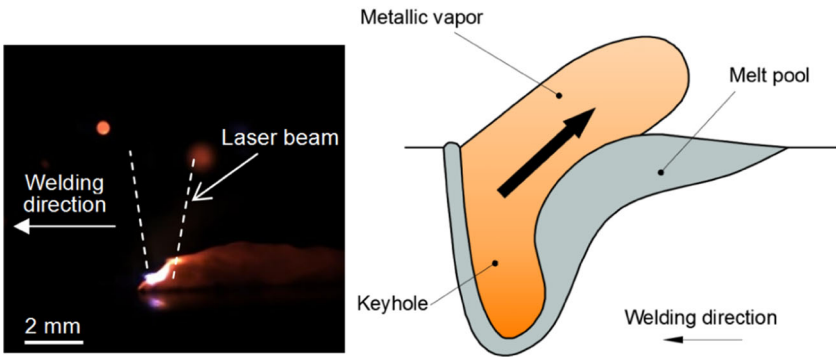

(b) 1.5 m/min ≤ v ≤ 3 m/min

Fig. 13 Images and schematic of weld pool, metallic vapor, and keyhole behaviors with respect to welding speed

5 Conclusions

In this paper, we conducted the experiments of autogenous laser welding on the stainless steel with 12-mm thickness has, and a 10-kW fiber laser was used throughout the experiments. We have drawn the following conclusions based on our observations and discussion on experimental results:

(1) The welding position affected autogenous laser welding of thick plates, and the preferable one was a 60° inclination angle between the incident laser beam and the gravity direction.
(2) A focal position below the workpiece surface helped to obtain a full penetration weld, since the inward convergent laser beam tended to be transmitted to a deeper keyhole. There existed affiliated relations of the formation of the underfill on the top surface with the generation of the root hump on the bottom surface and the escape of the pressurized energized vapor plume through the open keyhole.
(3) For the full penetration welds at a defocus of − 10 mm, the higher the welding speed was, the lower the underfill depth on the top surface was; this was due to the fact that the formation of a stable keyhole was accompanied by the stable weld pool and metallic vapor.
(4) The focal position or the welding speed could be optimized to reduce underfill defects to some extent. However, it was only feasible when a negative defocus was used; the combination of defocus value and the welding speed could be optimized to achieve a satisfactory appearance of welds.
(5) For the full penetration laser welding on thick plates, a bottom-shielding ambience helped to stabilize welding process, and obtain an excellent weld appearance on the top and bottom surfaces.

Acknowledgments The authors thank Prof. Zhuming Bi from Purdue University Fort Wayne for polishing the English.

Funding The authors are grateful to the financial support from the National Natural Science Foundation of China (No. 51605045, 51405034, 51641502), and the Natural Science Foundation of Hunan Province of China (No. 2015JJ3003).

References

1. Bachmann M, Avilov V, Gumenyuk A, Rethmeier M (2014) Experimental and numerical investigation of an electromagnetic weld pool support system for high power laser beam welding of austenitic stainless steel. J Mater Process Technol 214(3):578–591. https://doi.org/10.1016/j.jmatprotec.2013.11.013

2. Zhang M, Chen G, Zhou Y, Liao S (2014) Optimization of deep penetration laser welding of thick stainless steel with a 10 kW fiber laser. Mater Des 53:568–576. https://doi.org/10.1016/j.matdes.2013.06.066
3. Sokolov M, Salminen A, Katayama S, Kawahito Y (2015) Reduced pressure laser welding of thick section structural steel. J Mater Process Technol 219:278–285. https://doi.org/10.1016/j.jmatprotec.2014.12.026
4. Guo W, Liu Q, Francis JA, Crowther D, Thompson A, Liu Z (2015) Comparison of laser welds in thick section S700 high-strength steel manufactured in flat (1G) and horizontal (2G) positions. CIRP Ann Manuf Technol 64(1):197–200. https://doi.org/10.1016/j.cirp.2015.04.070
5. Shen XF, Li L, Guo W, Teng WH, He WP (2016) Comparison of processing window and porosity distribution in laser welding of 10 mm thick 30CrMnSiA ultrahigh strength between flat (1G) and horizontal (2G) positions. J Laser Appl 28:1–9
6. Sun J, Feng K, Zhang K, Guo B, Jiang E, Nie P, Huang J, Li Z (2017) Fiber laser welding of thick AISI 304 plate in a horizontal (2G) butt joint configuration. Mater Des 118:53–65. https://doi.org/10.1016/j.matdes.2017.01.015
7. Chen Z, Gao X, Katayama S, Xiao Z, Chen X (2017) Elucidation of high-power disk laser welding phenomena by simultaneously observing both top and bottom of weldment. Int J Adv Manuf Tech 88(1–4):1141–1150. https://doi.org/10.1007/s00170-016-8837-4
8. Feng J, Guo W, Irvine N, Li L (2016) Understanding and elimination of process defects in narrow gap multi-pass fiber laser welding of ferritic steel sheets of 30 mm thickness. Int J Adv Manuf Technol 88(5–8):1821–1830
9. Zhang LJ, Bai QL, Ning J, Wang A, Yang NJ, Yin XQ, Zhang JX (2016) A comparative study on the microstructure and properties of copper joint between MIG welding and laser–MIG hybrid welding. Mater Des 10:35–50
10. Guo W, Crowther D, Francis JA, Thompson A, Liu Z, Li L (2015) Microstructure and mechanical properties of laser welded s960 high strength steel. Mater Des 85:534–548. https://doi.org/10.1016/j.matdes.2015.07.037
11. Zhan X, Wang Y, Liu Y, Zhang Q, Li Y, Wei Y (2015) Investigation on parameter optimization for laser welded butt joint of TA15 alloy. Int J Adv Manuf Technol 84(9–12):1–10
12. Yang J, Gang S, Li X, Chen L, Xu F (2010) Typical joint defects in laser welding of aluminium–lithium alloy. In: Proc of the 36th International MATADOR, London, pp 595–598
13. Matsumoto N, Kawahito Y, Nishimoto K, Katayama S (2017) Effects of laser focusing properties on weldability in high-power fiber laser welding of thick high-strength steel plate. J Laser Appl 29(1):012003 **(9p)**. https://doi.org/10.2351/1.4966258
14. Li S, Chen G, Zhou C (2015) Effects of welding parameters on weld geometry during high-power laser welding of thick plate. Int J Adv Manuf Technol 79(1–4):177–182
15. Kashaev N, Ventzke V, Fomichev V, Fomin F, Riekehr S (2016) Effect of Nd: YAG laser beam welding on weld morphology and mechanical properties of Ti–6Al–4V butt joints and T-joints. Opt Lasers Eng 86:172–180
16. Fang XY, Liu H, Zhang JX (2015) Reducing the underfill rate of pulsed laser welding of titanium alloy through the application of a transversal pre-extrusion load. J Mater Process Technol 220:124–134
17. Fang XY, Zhang JX (2016) Microstructural evolution and mechanical properties in laser beam welds of Ti–2Al–1.5mn titanium alloy with transversal pre-extrusion load. Int J Adv Manuf Technol 85(1):337–343. https://doi.org/10.1007/s00170-015-7930-4
18. Zhang LJ, Zhang GF, Ning J, Zhang XJ, Zhang JX (2015) Microstructure and properties of the laser butt welded achieved at high welding speed. Mater Des 88:720–736. https://doi.org/10.1016/j.matdes.2015.09.072
19. Pan Q, Mizutani M, Kawahito Y, Katayama S (2016) High power disk laser–metal active gas arc hybrid welding of thick high tensile strength steel plates. J Laser Appl 28(1):012004. https://doi.org/10.2351/1.4934939
20. Kawahito Y, Mizutani M, Katayama S (2009) High quality welding of stainless steel with 10 kW high power fibre laser. Sci Technol Weld Join 14(4):288–294
21. Vänskä M, Abt F, Weber R, Salminen A, Graf T (2013) Effects of welding parameters onto keyhole geometry for partial penetration laser welding. Phys Procedia 41:199–208
22. Berger P, Hügel H, Graf T (2011) Understanding pore formation in laser beam welding. Phys Procedia 12:241–247
23. Jin X, Berger P, Graf T (2006) Multiple reflections and Fresnel absorption in an actual 3D keyhole during deep penetration laser welding. J Phys D Appl Phys 39(21):4703–4712
24. Zhang Y, Chen G, Wei H, Zhang J (2008) A novel 'sandwich' method for observation of the keyhole in deep penetration laser welding. Opt Laser Eng 46(2):133–139. https://doi.org/10.1016/j.optlaseng.2007.08.010
25. Zhang M, Chen G, Zhou Y, Li S (2013) Direct observation of keyhole characteristics in deep penetration laser welding with a 10 kW fiber laser. Opt Express 21(17):19997–20004. https://doi.org/10.1364/OE.21.019997
26. Zou JL, Wu SK, He Y, Yang WX, Xu JJ, Xiao RS (2015) Distinct morphology of the keyhole wall during high-power fiber laser deep penetration welding. Sci Technol Weld Join 20(8):655–658. https://doi.org/10.1179/1362171815Y.0000000049
27. Zou JL, Wu SK, Yang WX, He Y, Xu JJ, Xiao RS (2016) A novel method for observing the micro-morphology of keyhole wall during high-power fiber laser welding. Mater Des 89:785–790. https://doi.org/10.1016/j.matdes.2015.10.039
28. Kaplan AF (2012) Local absorptivity modulation of a 1 μm-laser beam through surface waviness. Appl Surf Sci 258(24):9732–9736. https://doi.org/10.1016/j.apsusc.2012.06.020
29. Kuryntsev SV, Gilmutdinov AK (2015) Heat treatment of welded joints of steel 0.3C–1Cr–1 Si produced by high-power fiber lasers. Opt Laser Technol 74:125–131. https://doi.org/10.1016/j.optlastec.2015.06.004
30. Zhang MJ, Chen GY, Zhou Y, Li SC, Deng H (2013) Observation of spatter formation mechanisms in high-power fiber laser welding of thick plate. Appl Surf Sci 280:868–875. https://doi.org/10.1016/j.apsusc.2013.05.081
31. Ilar T, Eriksson I, Powell J, Kaplan AFH (2012) Root humping in laser welding—an investigation based on high speed imaging. In: Laser Assisted Net Shape Engineering 7 (LANE 2012), Furth, Physics Procedia, vol 39. Elsevier, pp 27–32
32. Mei LF, Yan DB, Yi JM, Chen GY, Ge XH (2013) Comparative analysis on overlap welding properties of fiber laser and CO_2 laser for body-in-white sheets. Mater Des 49:905–912. https://doi.org/10.1016/j.matdes.2013.02.003
33. Vänskä M, Abt F, Weber R, Salmine A, Graf T (2013) Effects of welding parameters onto keyhole geometry for partial penetration laser welding. In: Lasers in Manufacturing (LiM 2013), Munich, Physics Procedia, vol 41. Elsevier, pp 199–208
34. Cheng Y, Jin X, Li S, Zeng L (2012) Fresnel absorption and inverse bremsstrahlung absorption in an actual 3D keyhole during deep penetration CO_2 laser welding of aluminum 6016. Opt Laser Technol 44(5):1426–1436. https://doi.org/10.1016/j.optlastec.2011.12.024
35. Rai R, Palmer TA, Elmer JW, Debroy T (2009) Heat transfer and fluid flow during electron beam welding of 304l stainless steel alloy. Weld J 88(3):54s–61s
36. Fabbro R (2010) Melt pool and keyhole behaviour analysis for deep penetration laser welding. J Phys D Appl Phys 43(44):445501 (9pp)
37. Pang S, Chen X, Shao X, Gong S, Xiao J (2016) Dynamics of vapor plume in transient keyhole during laser welding of stainless steel:

local evaporation, plume swing and gas entrapment into porosity. Opt Lasers Eng 82:28–40

38. Eriksson I, Powell J, Kaplan AFH (2011) Measurements of fluid flow on keyhole front during laser welding. Sci Technol Weld Join 16:636–641
39. Tan W, Shin Y (2014) Analysis of multi-phase interaction and its effects on keyhole dynamics with a multi-physics numerical model. J Phys D Appl Phys 47(34):345501 (17p). https://doi.org/10.1088/0022-3727/47/34/345501
40. Pang S, Chen X, Li W, Shao X, Gong S (2016) Efficient multiple time scale method for modeling compressible vapor plume dynamics inside transient keyhole during fiber laser welding. Opt Laser Technol 77:203–214